BJR

https://doi.org/10.1259/bjr.20220387

Received: 08 April 2022 | Revised: 19 September 2022 | Accepted: 17 October 2022 | Published online: 15 November 2022

Cite this article as:
Hu Z, Bieniosek M, Ferri V, Iagaru A, Kovalchuk N, Han B, et al. Image-mode performance characterisation of a positron emission tomography subsystem designed for Biology-guided radiotherapy (BgRT). *Br J Radiol* (2023) 10.1259/bjr.20220387.

FULL PAPER

# Image-mode performance characterisation of a positron emission tomography subsystem designed for Biology-guided radiotherapy (BgRT)

**[1]ZHIQIANG HU, [1]MATTHEW BIENIOSEK, [2]VALENTINA FERRI, [2]ANDREI IAGARU, [3]NATALIYA KOVALCHUK, [3]BIN HAN, [3]LEI XING, [3]LUCAS VITZTHUM, [1]PETER OLCOTT, [1]MANOJ NARAYANAN, [1]THOMAS LAURENCE, [3]YULAN REN, [1]OLUWASEYI M ODERINDE, [1]SHERVIN M SHIRVANI, [3]DANIEL CHANG and [3]MURAT SURUCU**

[1]RefleXion Medical, Inc, Hayward, CA
[2]Department of Radiology, Stanford University, Stanford, CA
[3]Department of Radiation Oncology, Stanford University, Stanford, CA

Address correspondence to: Dr Murat Surucu
E-mail: *surucu@stanford.edu*

**Objectives:** In this study, we characterise the imaging-mode performance of the positron emission tomography (PET) subsystem of the RefleXion X1 machine using the NEMA NU-2 2018 standard.
**Methods:** The X1 machine consists of two symmetrically opposing $90^0$ arcs of PET detectors incorporated into the architecture of a ring-gantry linear accelerator rotating up to 60 RPM. PET emissions from a tumour are detected by the PET detectors and used to guide the delivery of radiation beam. Imaging performance of the PET subsystem on X1 machine was evaluated based on sensitivity of the PET detectors, spatial resolution, count-loss performance, image quality, and daily system performance check.
**Results:** PET subsystem sensitivity was measured as 0.183 and 0.161 cps/kBq at the center and off-center positions, respectively. Spatial resolution: average FWHM values of 4.3, 5.1, and 6.7 mm for the point sources at 1, 10, and 20 cm off center, respectively were recorded. For count loss, max NECR: 2.63 kcps, max true coincidence rate: 5.56 kcps, and scatter fraction: 39.8%. The 10 mm sphere was not visible. Image-quality contrast values were: 29.6%, 64.9%, 66.5%, 81.8%, 81.2%, and background variability: 14.8%, 12.4%, 10.3%, 8.8%, 8.3%, for the 13, 17, 22, 28, 37 mm sphere sizes, respectively.
**Conclusions:** When operating in an imaging mode, the spatial resolution and image contrast of the X1 PET subsystem were comparable to those of typical diagnostic imaging systems for large spheres, while the sensitivity and count rate were lower due to the significantly smaller PET detector area in the X1 system. Clinical efficacy when used in BgRT remains to be validated.
**Advances in knowledge:** This is the first performance evaluation of the PET subsystem on the novel BgRT machine. The dual arcs rotating PET subsystem on RefleXion X1 machine performance is comparable to those of the typical diagnostic PET system based on the spatial resolution and image contrast for larger spheres.

## INTRODUCTION:

Over the past few decades, the decline in cancer incidence and mortality rates reflects the progression of new technologies targeting cancer treatment to increase curative strength.[1] To optimise the efficacy of radiotherapy, advanced treatment techniques that accurately identify and irradiate multiple target sites in real time at the optimal dose level are pursued. In addition, immobilisation devices and image guidance techniques are utilised to maintain minimal risk to the healthy structures surrounding the treatment target.[2,3]

A major technical limitation facing conventional image-guided radiation therapy (IGRT) is the inability to track real-time tumour motion during treatment delivery without a surrogate.[4,5] Organ movement, especially during respiration, can affect the precision of dose delivery to tumour, resulting in the irradiation of non-tumour and otherwise healthy tissues, which could lead to radiation toxicities.[6,7] Current external beam modalities also experience obstacles in the ablation of multiple tumour targets that move independently.[8] A new development came up with the integrating magnetic resonance imaging (MRI) system into a linac radiotherapy machine.[9,10] However, this development is accompanied with lorentz force distorting the lateral therapeutic beam penumbra which is significant in small treatment field. Also, MR images are susceptible to distortions based on patient chemical composition, which can in

turn increase the localisation uncertainty. In addition, radiofrequency energy emitted from MR generates heat in the body which could go above the specific absorption rate (SAR) limit.[11]

The advent of molecular imaging, such as positron emission tomography (PET), opens an avenue to visualise and quantify oncological diseases on molecular level. On the molecular level, you have access to tumour metabolic activities or biochemical information, which is useful in tumour diagnosis, delineation, treatment delivery guidance and tumour response assessment after treatment [81213] The RefleXion™ X1 machine (RefleXion Medical, Inc., Hayward, CA) is a hybrid imaging-therapy system that is designed to address challenges in radiation oncology using biology-guided radiotherapy (BgRT), a novel radiotherapy technique that aims to improve the conformality and precision with which external beam radiotherapy is delivered to malignant lesions, including those that are in motion. The first X1 machine was installed at the Stanford Medicine.

This novel radiotherapy platform incorporates PET and computed tomography (CT) technologies into the architecture of a ring-gantry linear accelerator system. The PET subsystem measures the radioactivity per unit volume and provide a semi-quantitative standard uptake value (SUV) of the injected radiotracer. These measurements are decay-corrected and normalised based on the body weight and injected activity.[14] Unlike a conventional PET scanner mounted with a fixed 360° ring, this novel PET subsystem comprises two symmetrically movable opposing $90^0$ arcs, which acquires annihilation photons of $180^0$ around the target at once. Earlier work on rotating dual PET arc (prototype design) demonstrated that for a fixed number of detectors, the rotating dual PET arc has a higher sensitivity than corresponding fixed ring PET system due to fixed ring PET system having smaller number of active line-of-response (LOR).[15] However, in reality, the numbers of detectors are not the same, limiting the sensitivity and count rate performance of X1 compared to a full-ring diagnostic PET scanner.

Another study demonstrated the capabilities of using rotating dual PET diagnostic system (asymmetrical PET arc rotating at 30 rpm) in both a research and clinical ecosystem.[16] Although the PET system on X1 machine uses a symmetrical arc rotating at 60 rpm, achieving a better sensitivity and count rate performance.

While the PET subsystem of the RefleXion X1 machine is primarily designed for beamlet delivery guidance in real time, PET images acquired in imaging mode during PET simulation on RefleXion X1, are utilised to confirm the characteristics of the tumour such as activity concentration and tumour PET signal contrast to the background. The images acquired on RefleXion X1 during are also used to develop the actual BgRT treatment plan. On the day of each BgRT treatment fraction, FDG is injected to the patient and then a short PET pre-scan is conducted to confirm that the emissions coming from the target region match what is expected by the treatment plan (within expected tolerances). If any of the pre-defined criteria are not met, then the operator will be informed that a BgRT treatment cannot be delivered that day. In addition, images derived from real-time treatment are useful for quality assurance in asserting biomarker's distribution during treatment delivery. Hence, it becomes necessary to evaluate RefleXion X1's imaging subsytem performance using a national standard and compare it to other diagnostic PET systems.

The National Electrical Manufacturers Association (NEMA) published a universal measurement procedure to have a standardised set of experiments and quantify the performance of a PET system. The results thereof are to serve as a method to compare the different performance levels for different PET systems.[17] In this study, the performance of the X1 PET subsystem in imaging mode (without any treatment beam delivery) was evaluated according to the NEMA NU 2–2018 standards.[17] The description of real-time PET guidance combined with beamlet delivery and its performance validation through dosimetric evaluation is published separately[18] .

## METHODS AND MATERIALS

### X1 machine PET subsystem 1.0

The X1 machine PET subsystem is mounted on the ring gantry in the same plane as the 6 MV treatment beam linear accelerator, as shown in Figure 1. It consists of two symmetrically opposing $90^0$ arcs of PET detectors, covering approximately $180^0$ (50%) of the ring gantry. Each PET arc has 32 detectors, and each detector is made of 12 × 6 Lutetium-based scintillator arrays with each crystal size of 4.14 × 4.14 × 20 mm that is directly coupled to a silicon photomultiplier (SiPM) array (MPPC, Hamamatsu Photonics). The inner diameter of the PET from scintillator to scintillator is approximately 1066 mm. The single bed image field-of-view (FOV) is 50.0 cm in diameter and 5.2 cm in axial length.

The PET subsystem includes an embedded $^{22}$Na check source (Activity is approx. 3.7 MBq at the time of installation) beneath the covers for quality assurance and to ensure real-time safety of the system. Periodic monitoring of the check source location in sinogram space ensures the proper functioning of PET detectors. The PET arc radiation sensitive electronics is located adjacent to the scintillator and SiPMs, behind 2-cm-thick lead shielding to protect them from the high energy scattered X-rays from the Linac beam. Also, lead shielding reduces the out-of-field γ photons from reaching the scintillation crystals.

*PET Data acquisition:* The data acquisition of the PET detector converts the proportional electronic signal current generated in SiPM into a singles event that encodes the location of the event (which crystal was hit), the energy of the event (how many optical photons were recorded), and the time of the event. Singles events are processed, and coincidence events were subsequently selected by the data acquisition for image reconstruction. Random coincidence events are collected using traditional delayed window approach. Random correction is performed by subtracting Gaussian smoothed random data in sinogram space. While no specific scatter correction is applied to the PET data due to the speed constraint of the delivery algorithm, a fraction of scatter events is excluded by applying a 395 keV to 600 keV energy window.

Figure 1. Layout of the PET arcs in the gantry (dimensions are in mm)

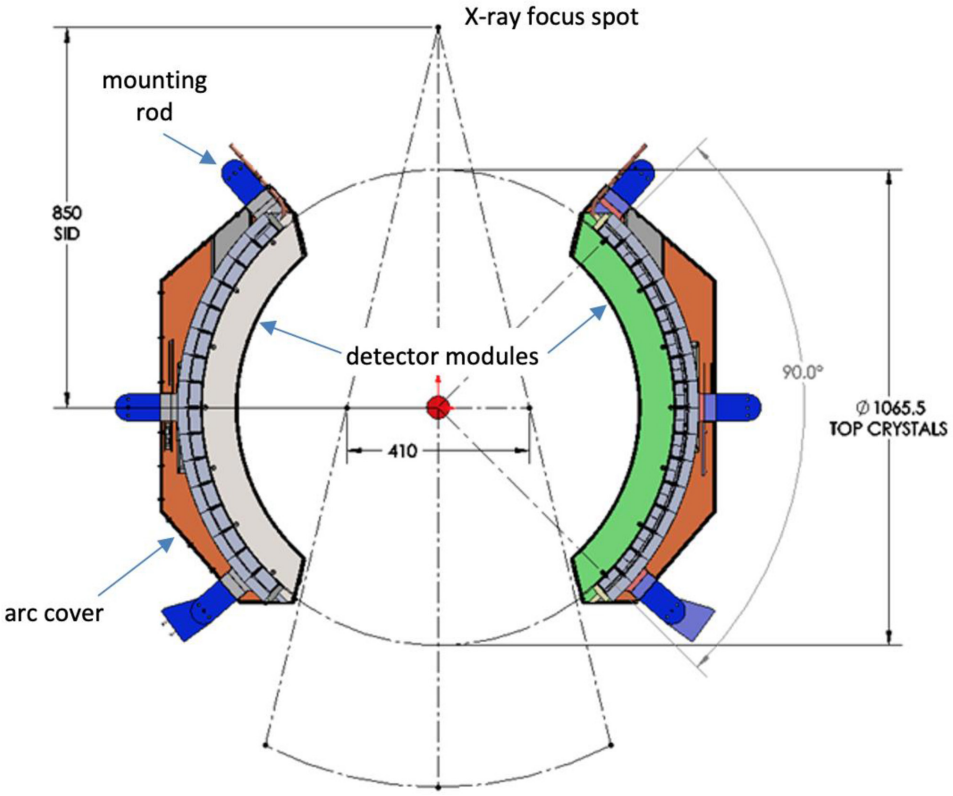


*PET normalisation*: A component-based approach is used for PET detector normalisation, consisting of geometric, axial, and re-binning factors.[19] The normalisation factors for the PET detectors were generated using a Ge-68 rod source (Activity is approx. 24.3 MBq) inserted into the phantom holder hole 30 cm away from the centre of the axial FOV. 30 M coincidence events were collected, which provided sufficient data statistics.

*PET activity concentration calibration:* The PET activity concentration calibration was performed using a uniform cylinder (Jaszczak phantom from Data Spectrum with inserts removed). The phantom centred on the couch was filled with FDG activity between 18.5 MBq and 74.0 MBq at the start of PET acquisition.

*Image correction and reconstruction:* For spatial resolution and image quality measurement, a filtered back-projection reconstruction with Hanning-filter was performed on the collected coincidence data after single slice re-binning.[18] The conversion of 3D to 2D data was deemed sufficient in preserving image quality due to the system's short axial FOV of 5.3 cm in IEC-Y axis, with the benefit of speeding up reconstruction. The data were corrected for random, decay, and attenuation, but not for scatter. For random correction, a delayed window approach was used to collect random coincidence events which were then smoothed in sinogram space using a gaussian filter prior to subtraction from the prompt sinograms. For attenuation correction, the simulation CT image was converted to a PET attenuation map at 511 keV.[20]

The reconstruction algorithm and data correction methods are kept consistent between imaging and delivery modes. For BgRT to be effective, the algorithm must use a linear and analytic method to reconstruct PET data. FBP is chosen mainly because of its speed performance. As far as scatter correction is concerned, it is not implemented due to the need of speed performance for real-time delivery.

## NEMA NU-2018 performance measurement

### *Sensitivity*

Sensitivity is a measure that assesses the total coincidence events detected for a given source in a PET system. To achieve this, the NEMA PET sensitivity phantom consisting of five concentric aluminium sleeves of 70 cm length as described in NEMA NU-2 2018 was utilised. A 70-cm-long capillary tube was filled with an F-18 FDG solution and inserted in the smallest diameter aluminium sleeve. The set of sleeves was placed along the axial direction of the PET, centred or 10 cm off centre in the transverse FOV for measuring sensitivity at centre or off centre, respectively. The activity in the tube at the start of data acquisition was below 44.4 MBq.

### *Spatial resolution*

The ability of the PET system to differentiate between two points after image reconstruction was tested by measuring the radial, tangential, and axial resolutions of FDG point sources in the air. The prepared point sources were approximately 1 mm in axial length, which was embedded at the tip of a capillary tube with an inner diameter of 0.9–1.1 mm placed on the spatial resolution

adaptor. Six point sources were arranged horizontally 1 cm, 10 cm, and 20 cm away from the centre axis, three in the iso-plane, and the other three off the iso-plane by 3/8 axial FOV. All six point sources were measured simultaneously for 10 min, and the measured data were reconstructed with filtered back projection (FBP) algorithm on voxels of 1.15 × 1.15 × 2.1 $mm^3$ each, where the voxel's axial dimension was 2.1 mm. No post-filtering was applied on the reconstructed images.

### *Count-loss*

A cylindrical NEMA scatter phantom of 70 cm long and 20 cm diameter cylinder was used to measure the count-loss performance of the PET. A 70-cm-long capillary tube was inserted into the scatter phantom. The tube was filled with a high concentration of FDG, approximately 259 MBq at the start of PET scanning. During the PET data acquisition, the scatter phantom was positioned at the centre of the transverse FOV, while the tube was 4.5 cm below the centre of the scatter phantom. A total of 20 frames of PET data were collected, 2M coincidence events each and 15 min between two consecutive frames. The counting rates for random, scatter, and true coincidence events were calculated using the method provided in NEMA NU-2 2018.

### *Image quality*

The image contrast and background variability were evaluated using the NEMA body and scatter phantom sets containing six fillable spheres with a diameter of 10, 13, 17, 22, 28, and 37 mm and Styrofoam beads mixed with water at the centre (to mimic the lung). All the spheres were filled with diluted FDG activity concentration, and the NEMA body phantom alongside the lung insert was filled with lower FDG activity concentration to achieve a sphere-to-background activity concentration ratio (SBR) of 4:1. This is similar to the contract-to-noise ratio (CNR) in order to achieve an improved image quality within the short FOV of the PET system.[18] The activity concentration in the body phantom (background) was about 4.7 kBq/ml at the start of PET scanning. The body phantom was positioned on the couch per NEMA standard and centred in the transverse FOV of PET subsystem. The scatter phantom (count-loss cylinder) was placed against the body phantom to simulate the activity outside the axial FOV in a clinical scenario. During the operation, the PET detectors rotated axially around the phantom as the phantom was stepped cranio-caudally through the bore of the device with a step size of 2.1 mm and a 10 s stationary scan after each step. Four passes back-and-forth were conducted with 40 steps each. A filtered back-projection reconstruction with Hanning-filter was performed on the collected coincidence data after single slice re-binning. The voxel size used in the reconstruction was 2.0 × 2.0 × 2.1 $mm^3$, with the axial dimension being 2.1 mm. The reconstructed images were smoothed using a Gaussian filter with a standard deviation of 5 mm both axially and in plane.

### *Daily system performance check*

The daily performance check of the PET subsystem centres on the system's energy and time resolution. The energy and time resolution were tested using a point source ($^{22}Na$) inserted at the centre of a Universal Multimodality Alignment (UMA) cube. The PET data from the point source at the centre of the cube were recorded and evaluated.

Figure 2. PET image of a uniform cylinder (a Jaszczak phantom with inserts removed).

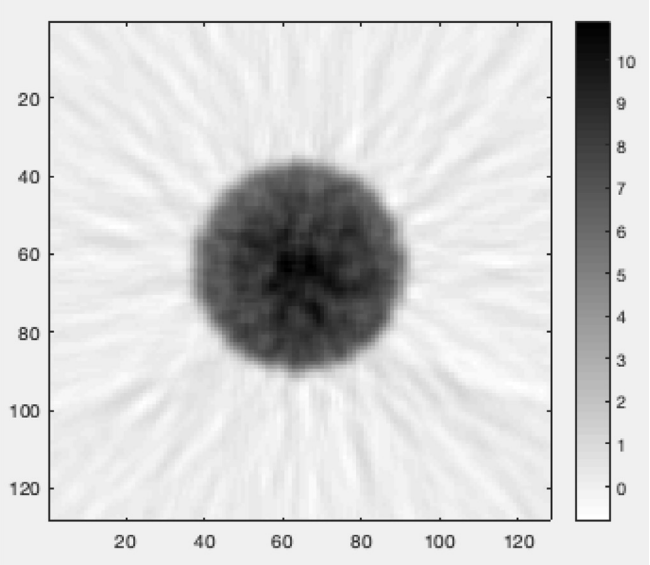


## RESULTS

This study details the imaging performance evaluation of the PET subsystem of the RefleXion X1 machine using the NEMA NU-2 2018 standard measurements. Normalisation factors for the PET detectors were generated, and PET images of the uniform phantom (a Jaszczak phantom with inserts removed) were shown to be uniform without ring artefacts as demonstrated in the example image in Figure 2. The activity concentration error of the PET subsystem was found to be 9.7% which was less than the 10% factory-specified limit. The count rate capability test showed that the PET subsystem was able to successfully process at least 35k coincidence events per second.

### Sensitivity

The average total sensitivity of the X1 PET subsystem was measured to be 0.183 and 0.161 cps/kBq at the centre of the transverse FOV and 10 cm off-centre, respectively.

### Spatial resolution

Table 1 shows the axial, tangential, and radial spatial resolutions at 1, 10, and 20 cm offset using the NEMA NU-2 2018 standard. The average spatial resolutions were measured as 4.3, 5.1, and 6.7 mm in FWHM for 1, 10, and 20 cm offsets, respectively.

### Count loss

The count loss for the RefleXion X1 PET was assessed using 20 scanned frames, 2M coincidence events each, with a 15-min interval between scans. The scans exhibit a max noise equivalent count-rate (NECR) of 2.6 kcps/kBq/ml, true count rate of 5557 counts, and scatter fraction of 40.0% shown in Figure 3. Due to the computer hardware constraint associated with data processing, the counting performance of the Reflexion PET will saturate when the singles count rate is beyond 7 M/s. What is reported is the performance numbers that are achievable with the Reflexion PET.

Table 1. The measured NEMA NU2-20218 spatial resolutions

| Offset Distance (cm) | FWHM (mm) | | | |
|---|---|---|---|---|
| | Axial | Tangential | Radial | Average (Product Tolerances) |
| 1 | 4.23 | 4.31 | 4.27 | 4.27 (< 5.50) |
| 10 | 5.24 | 4.80 | 5.18 | 5.07 (< 6.00) |
| 20 | 7.02 | 5.78 | 7.15 | 6.65 (< 7.00) |

### Image quality

Figure 4 shows the acquired PET image of the NEMA IEC body phantom. Table 2 shows the image contrast and background variability measurements collected for five spheres filled with an FDG solution at a 4:1 sphere-to-background concentration ratio. Note that the smallest sphere (10 mm in diameter) is not included for evaluation due to statistical noise, as can be seen from the slice going through the sphere centres.

### System performance check

The PET SPC test measured over 77 days shows a median energy and time resolution of 7.84% (range: 6.25–10.18%) and 784.0 ps (753.3 ps- 805.9 ps), respectively, for the PET system Figure 5. The QA limit for energy resolution was 15% and 1000 ps for the time resolution. The median kVCT localisation offset from the laser alignment was 0.4 mm (range: 0to 2.9 mm). The kVCT and PET isocentre coincidence was less than 1 mm for the 77 day measurement.

## DISCUSSION

The RefleXion X1 machine is the first linear accelerator equipped with PET detectors that are designed to detect the annihilation photons from the tumour for BgRT. This is the first report to characterise the integrated PET subsystem. However, a NEMA standardised performance measurement for a rotating PET system with 180° angular coverage is not available. The authors believe that the NEMA NU 2–2018 standards can be utilised in the meantime, since it is the industry standard for stationary 360° diagnostic PET systems and a rotating PET is geometrically equivalent to a stationary full-ring PET.

However, since the primary function of the PET subsystem is to satisfy the tumour tracking needs for real-time therapeutic beam delivery and not to mimic the diagnostic system, the imaging performance evaluation should come from radiation oncology needs, not necessarily from diagnostic radiology requirements.

### Sensitivity

Table 3 shows the sensitivity performance of the rotating partial RefleXion PET system compared to the stationary full PET system of Philips Vereos[21], GE Discovery MI[22], Siemens Biograph Vision[23] and Toshiba Celesteion[24]. Sensitivity performance of the RefleXion PET system is lower than diagnostic PET systems due to the smaller axial FOV (AFOV) and the two 90° arc design of the RefleXion system.

### Spatial resolution

The RefleXion PET system using the NEMA-Standard achieves a comparable spatial resolution, which is similar to the diagnostic system results as shown in Table 4. Alongside the count statistics, crystal size is a factor that determines the intrinsic spatial resolution of the PET system.

### Count Loss

The count-loss performance has only been characterised to around 12.5 kBq/ml due to the hardware limitations in

Figure 3. PET Count-loss performance measured according to NEMA NU-2 2018 (Due to the computer hardware constraint associated with data processing, the counting performance of the Reflexion PET will saturate when the count rate is beyond certain number. What is reported is the performance numbers that are achievable with the Reflexion PET.)

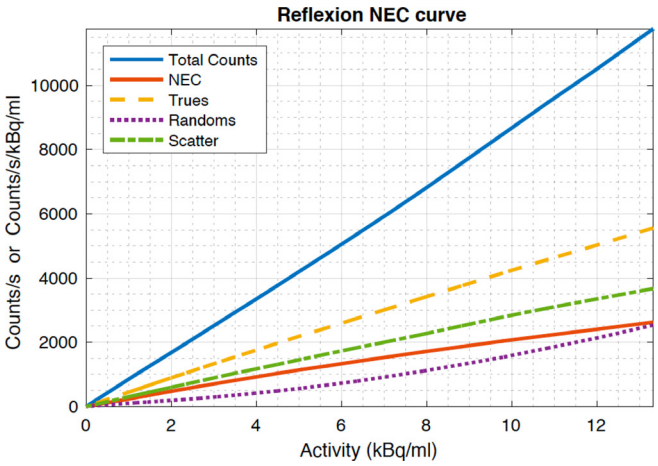


Figure 4. PET image quality evaluation- NEMA NU-2 2018

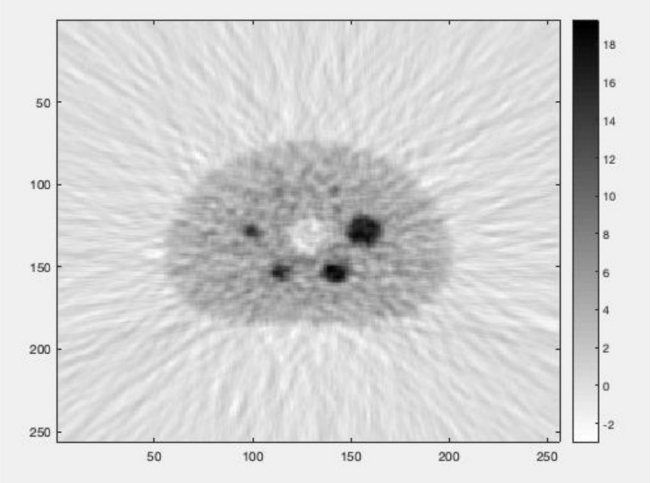

Table 2. Image contrast and background variability of the X1 PET subsystem following NEMA NU-2 2018. RefleXion specified tolerance for both image contrast and background variability is given in parenthesis

| Sphere Diameter (mm) | Image Contrast % | Background Variability % |
|---|---|---|
| 13 | 29.6 (> 25) | 14.8 (< 17) |
| 17 | 64.9 (> 30) | 12.4 (< 15) |
| 22 | 66.5 (> 35) | 10.3 (< 12) |
| 28 | 81.8 (> 45) | 8.8 (< 12) |
| 37 | 81.2 (> 50) | 8.3 (< 10) |

processing singles events, above which the PET subsystem will be saturated. As a result, one does not see a NECR peak and then drop-off as the activity increases on the Reflexion PET, as expected from a typical diagnostic PET (Table 5). Note however that in normal operation, which very well covers the system's operating activity range, the Reflexion PET has a fairly linear counting performance.

## Image quality

Despite the fact that RefleXion PET system is not designed as a diagnostic system, it shows a good image contrast recovery comparable to the high-end diagnostic PET systems as shown in Table 6. The choice of reconstruction method has an impact on the image contrast, especially for the small sphere diameter of 10 mm. RefleXion PET system generated more statistical noise using a FBP for reconstruction method while Siemens Biograph Vision image contrast measurement for the 10 mm sphere has a unusual high contrast (Table 6), which is possibly, besides its superior spatial resolution, caused by Gibbs artefact from the point-spread function (PSF) reconstruction method.[23] A study has suggested the use of more iterations to improve the contrast recovery, however, it might also increase the background variability.[25] A penalised-likelihood iterative PET reconstruction has recently been introduced by GE Healthcare in their commercial software, termed Q.Clear. It models PSF to enhance image contrast and simultaneously controls the noise through the use of a penalty term.[25] Therefore, image reconstruction optimisation is necessary for achieving a good image contrast, while reducing the background variability. It is possible that in the future, a GPU-based reconstruction using more advanced yet more time-consuming algorithms can be implemented on Reflexion PET for its real-time radiotherapy application.

## System performance check

Initially the PET daily tests were performed on only the dates that the PET system was used for clinical use. Later, the PET SPC tests were repeated more frequently to assess system variance, (77 times in 9 months). The daily results were all within the limits that was established by the QA team, including the alignment of PET/kVCT

Figure 5. SPC test for 77 days (a) Uncorrected energy resolution (red line indicate the pass mark <15%) and (b) Time resolution (red line indicate the pass mark pass <1000ps)

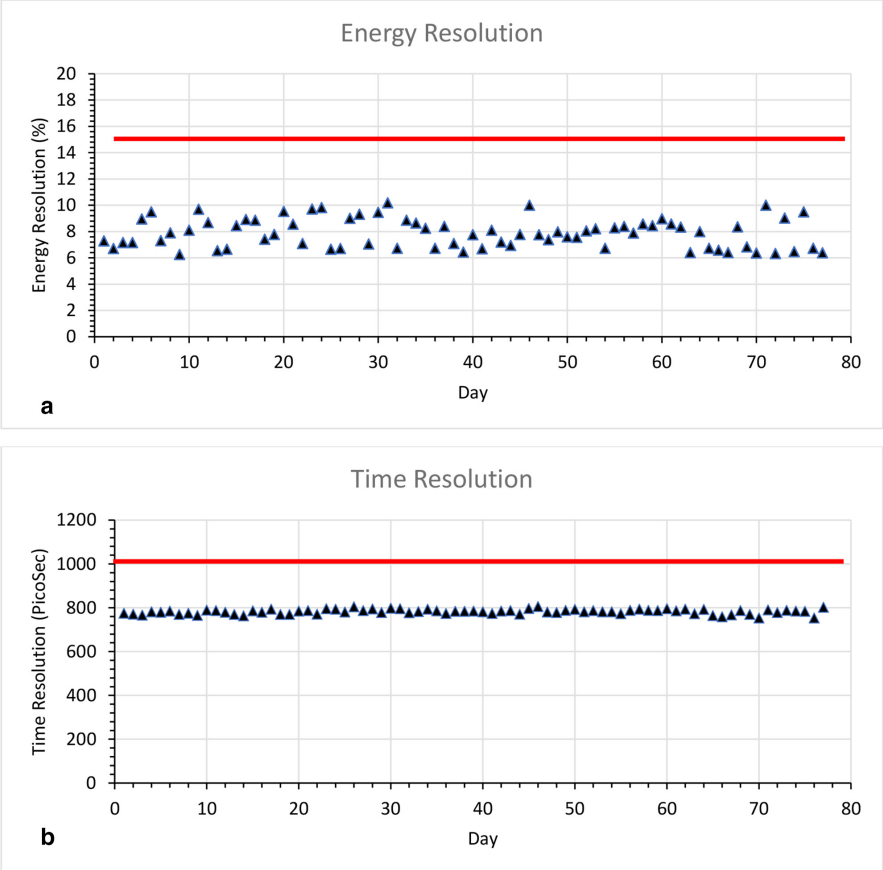

Table 3. A Sensitivity performance of the RefleXion, Vereos, Discovery MI, Vision and Celesteion

| PET system | Axial FOV (cm) | Sensitivity at Centre of transverse FOV (cps/kBq) | Sensitivity at 10 cm off-centre (cps/kBq) |
|---|---|---|---|
| RefleXion | 5.2 | 0.183 | 0.161 |
| Philips-Vereos | 16.4 | 5.10 | 5.20 |
| GE- Discovery MI | 20.0 | 13.4 | 14.0 |
| Siemens- Biograph Vision | 25.6 | 16.4 | 16.3 |
| Toshiba- Celesteion | 19.6 | 3.8 | 3.8 |

Table 4. Comparison of spatial resolution measurements

| PET System (crystal size) | 1 cm | | | 10 cm | | | 20 cm | | |
|---|---|---|---|---|---|---|---|---|---|
| | FWHM | | | FWHM | | | FWHM | | |
| | Axial | Tangential | Radial | Axial | Tangential | Radial | Axial | Tangential | Radial |
| RefleXion (4.1 × 4.1x 20 $mm^3$) | 4.2 | 4.3 | 4.3 | 5.2 | 4.8 | 5.2 | 7.0 | 5.8 | 7.2 |
| Vereos (4 × 4 x 19 $mm^3$) | 4.2 | N/A | N/A | 4.4 | 4.0 | 4.0 | 4.6 | 4.9 | 5.8 |
| Discovery MI (3.95 × 5.3×25 $mm^3$) | 4.4 | 4.0 | 4.0 | 5.5 | 4.2 | 5.3 | 5.7 | 4.7 | 7.5 |
| Vision (3.2 × 3.2 x 25 $mm^3$) | 3.5 | 3.5 | 3.6 | 4.3 | 3.9 | 4.5 | 4.4 | 3.5 | 5.8 |
| Celesteion (4 × 4 x 4 $mm^3$) | 4.4 | 4.7 | 4.5 | 4.6 | 4.8 | 4.6 | 4.7 | 5.3 | 5.8 |

isocentre and PET energy resolution and time-of -flight resolution measurements. The unusual small values of energy resolution are due to two reasons. The first has to do with a simple energy calibration approach that is taken: only one data point, the 511 keV peak, is used and a linear fit is assumed. In reality, for SiPM based systems, the energy calibration is non-linear due to multiple hits of scintillation photons on a single cell. The second reason why the measured energy resolution value is small is the system currently collects only Photopeak events and does not perform detector Compton scatter summing for simplicity. This is the first performance evaluation of the dual-arc PET subsystem on the X1 radiotherapy machine. The primary function of the PET subsystem is to satisfy the tumour tracking needs for real-time therapeutic beam delivery and not to mimic the diagnostic system. Therefore, the imaging performance evaluation should come from radiation oncology needs, not necessarily from diagnostic radiology requirements.

In this study, the reconstruction algorithm for the PET subsystem on the X1 radiotherapy machine corrected for random, decay, and attenuation. Future study will investigate the reconstruction algorithm with scatter correction and account for speed performance which is essential to real-time

Table 5. Count- Loss performance

| PET system | Max NECR (kcps/kBq/ml at kBq/ml) | Scatter Fraction (%) at Max NECR |
|---|---|---|
| RefleXion | 2.6 at (peak not reached) | 40.0 |
| Philips-Vereos | 153.4 at 54.9 | 33.9 |
| GE- Discovery MI | 201.1 at 22.1 | 40.4 |
| Siemens- Biograph Vision | 306.0 at 32.6 | 38.7 |
| Toshiba- Celesteion | 70.0 at 29.6 | 37.3 |

Table 6. Image contrast and background variability for different sphere diameters (whole-body PET), with sphere-to-background ratio of 4:1

| PET system | | Image Contrast % (Background Variability%) | | | | |
|---|---|---|---|---|---|---|
| | 10 mm | 13 mm | 17 mm | 22 mm | 28 mm | 37 mm |
| RefleXion | N/A | 29.6 (14.8) | 64.9 (12.4) | 66.5 (10.3) | 81.8 (8.8) | 81.2 (8.3) |
| Philips-Vereos | 38.4 (8.4) | 61.3 (7.1) | 65.9 (5.9) | 68.5 (4.6) | 83.4 (3.5) | 86.4 (2.8) |
| GE-Discovery MI | 51.7 (10.0) | 61.5 (7.8) | 66.2 (6.0) | 81.3 (3.8) | 86.6 (3.8) | 90.0 (3.0) |
| Siemens-Biograph Vision | 93.1 (6.4) | 73.5 (5.0) | 79.0 (4.0) | 87.0 (3.1) | 86.3 (2.7) | 89.4 (2.2) |
| Toshiba- Celesteion | 27.9 (6.2) | 48.6 (5.3) | 52.0 (4.6) | 60.5 (4.1) | 72.9 (3.9) | 77.1 (3.8) |

usage of the PET subsystem in the radiotherapy clinical environment.

## CONCLUSION

A dual-arc, rotating PET subsystem incorporated into ring-gantry LINAC architecture was developed for BgRT and its imaging performance was evaluated using the NEMA NU-2 2018 standard. When operating in an imaging mode, spatial resolution and image contrast were comparable to those of typical diagnostic PET systems, while sensitivity and count rate were lower. Notably, the sensitivity and count rate were expected to be lower due to design of the system which requires a far smaller detector area than a typical diagnostic system. Clinical efficacy when used in BgRT remains to be validated.

## REFERENCES


1. Siegel RL, Ma J, Zou Z, Jemal A. Cancer statistics, 2014. *CA Cancer J Clin* 2014; **64**: 9–29. https://doi.org/10.3322/caac.21208
2. Brahme A. Development of radiation therapy optimization. *Acta Oncol* 2000; **39**: 579–95. https://doi.org/10.1080/028418600750013267
3. Thondykandy BA, Swamidas JV, Agarwal J, Gupta T, Laskar SG, Mahantshetty U, et al. Setup error analysis in helical tomotherapy based image-guided radiation therapy treatments. *J Med Phys* 2015; **40**: 233–39. https://doi.org/10.4103/0971-6203.170796
4. Oderinde OM, Shirvani SM, Olcott PD, Kuduvalli G, Mazin S, Larkin D. The technical design and concept of a PET/CT linac for biology-guided radiotherapy. *Clin Transl Radiat Oncol* 2021; **29**: 106–12. https://doi.org/10.1016/j.ctro.2021.04.003
5. Cerviño LI, Du J, Jiang SB. Mri-Guided tumor tracking in lung cancer radiotherapy. *Phys Med Biol* 2011; **56**: 3773–85. https://doi.org/10.1088/0031-9155/56/13/003
6. Ting L-L, Chuang H-C, Liao A-H, Kuo C-C, Yu H-W, Tsai H-C, et al. Tumor motion tracking based on a four-dimensional computed tomography respiratory motion model driven by an ultrasound tracking technique. *Quant Imaging Med Surg* 2020; **10**: 26–39. https://doi.org/10.21037/qims.2019.09.02
7. Rietzel E, Chen GTY, Choi NC, Willet CG. Four-Dimensional image-based treatment planning: target volume segmentation and dose calculation in the presence of respiratory motion. *Int J Radiat Oncol Biol Phys* 2005; **61**: 1535–50. https://doi.org/10.1016/j.ijrobp.2004.11.037
8. Shirvani SM, Huntzinger CJ, Melcher T, Olcott PD, Voronenko Y, Bartlett-Roberto J, et al. Biology-guided radiotherapy: redefining the role of radiotherapy in metastatic cancer. *Br J Radiol* 2021; **94**(1117): 20200873. https://doi.org/10.1259/bjr.20200873
9. Snyder JE, St-Aubin J, Yaddanapudi S, Boczkowski A, Dunkerley DAP, Graves SA, et al. Commissioning of a 1.5T elekta unity MR-linac: a single institution experience. *J Appl Clin Med Phys* 2020; **21**: 160–72. https://doi.org/10.1002/acm2.12902
10. Klüter S. Technical design and concept of a 0.35 T MR-Linac. Clin Transl Radiat Oncol. Internet]. 2019. Available from: https://linkinghub.elsevier.com/retrieve/pii/S2405630819300692
11. Thorwarth D, Low DA. Technical challenges of real-time adaptive MR-guided radiotherapy. *Front Oncol* 2021; **11**: 634507. https://doi.org/10.3389/fonc.2021.634507
12. Zhu A, Lee D, Shim H. Metabolic positron emission tomography imaging in cancer detection and therapy response. *Semin Oncol* 2011; **38**: 55–69. https://doi.org/10.1053/j.seminoncol.2010.11.012
13. Ganem J, Thureau S, Gardin I, Modzelewski R, Hapdey S, Vera P. Delineation of lung cancer with FDG PET/CT during radiation therapy. *Radiat Oncol* 2018; **13**: 219. https://doi.org/10.1186/s13014-018-1163-2
14. Miwa K, Wagatsuma K, Iimori T, Sawada K, Kamiya T, Sakurai M, et al. Multicenter study of quantitative PET system harmonization using NIST-traceable 68ge/68ga cross-calibration kit. *Physica Medica* 2018; **52**: 98–103. https://doi.org/10.1016/j.ejmp.2018.07.001
15. Townsend D, Byars L, Defriset M, Geissbuhler A, Nutt R. Rotating positron tomographs revisited. *Phys Med Biol* 1994; **39**: 401–10. https://doi.org/10.1088/0031-9155/39/3/008
16. Townsend DW, Beyer T, Meltzer CC, Dachille MA, Derbyshire SWG, Jones AKP, et al. The ECAT ART scanner for positron emission tomography. 2. research and clinical applications. *Clin Positron Imaging* 1999; **2**: 17–30. https://doi.org/10.1016/s1095-0397(98)00056-9
17. NEMA. *NEMA Standards Publication NU 2-2018: Performance Measurements of Positron Emission Tomographs*. Rosslyn, VA; Report No: National Electrical Manufacturers Association; 2018.
18. Narayanan M, Zaks D, Olcott P, Voronenko Y, Burns J, Xu S, et al. Physical validation of biology-guided radiotherapy for delivering a tracked dose distribution to a moving PET-avid target. *International Journal of Radiation Oncology*Biology*Physics* 2021; **111**: S22. https://doi.org/10.1016/j.ijrobp.2021.07.078
19. Bailey DL, Townsend DW, Kinahan PE, Grootoonk S, Jones T. An investigation of factors affecting detector and geometric correction in normalization of 3-D PET data. *IEEE Trans Nucl Sci* 1996; **43**: 3300–3307. https://doi.org/10.1109/23.552739
20. Bai C, Shao L, Da Silva AJ, Zhao Z. n.d.).( A generalized model for the conversion from CT numbers to linear attenuation coefficients. *IEEE Trans Nucl Sci*. Available from: https://ieeexplore.ieee.org/document/1236959/
21. Rausch I, Ruiz A, Valverde-Pascual I, Cal-González J, Beyer T, Carrio I. Performance evaluation of the vereos PET/CT system according to the NEMA NU2-2012 standard. *J Nucl Med* 2019; **60**: 561–67. https://doi.org/10.2967/jnumed.118.215541
22. Hsu DFC, Ilan E, Peterson WT, Uribe J, Lubberink M, Levin CS. Studies of a next-generation silicon-photomultiplier-based time-of-flight PET/CT system. *J Nucl Med* 2017; **58**: 1511–18. https://doi.org/10.2967/jnumed.117.189514
23. Schaar J, Noordzij W, Dierckx R, et al. Performance characteristics of the digital biograph vision PET/CT system. *J Nucl Med [Internet]* 2019. Available from: http://jnm.snmjournals.org/lookup/doi/10.2967/jnumed.118.215418
24. Kaneta T, Ogawa M, Motomura N, Iizuka H, Arisawa T, Hino-Shishikura A, et al. Initial evaluation of the celesteion large-bore PET/CT scanner in accordance with the NEMA NU2-2012 standard and the japanese guideline for oncology FDG PET/CT data acquisition protocol version 2.0. *EJNMMI Research* 2017; **7**(1): 83. https://doi.org/10.1186/s13550-017-0331-y
25. Chen S, Hu P, Gu Y, Yu H, Shi H. Performance characteristics of the digital umi550 PET/CT system according to the NEMA NU2-2018 standard. *EJNMMI Phys* 2020; **7**: 43. https://doi.org/10.1186/s40658-020-00315-w